# PIV and topographic analysis data from analogue experiments involving 3D structural inheritance and multiphase rifting (https://doi.org/10.5880/fidgeo.2021.042)

Zwaan, F.[1], Chenin, P.[2], Erratt, D.[2], Manatschal, G.[2], & Schreurs, G.[1]

1. *University of Bern, Institute of Geological Sciences, Baltzerstrasse 1+3, 3012 Bern, Switzerland*
2. *Université de Strasbourg, CNRS, ENGEES, ITES UMR 7063, 5 rue Descartes, Strasbourg F-67084, France*

## 1. Licence



## 2. Citation

**When using the data please cite:**

Zwaan, F., Chenin, P., Erratt, D., Manatschal, G., & Schreurs, G. (2021). PIV and topographic analysis data from analogue experiments involving 3D structural inheritance and multiphase rifting. GFZ Data Services. https://doi.org/10.5880/fidgeo.2021.042

**The data are supplementary material to:**

Zwaan, F., Chenin, P., Erratt, D., Manatschal, G., & Schreurs, G. (2021). Competition between 3D structural inheritance and kinematics during rifting: Insights from analogue models. Basin Research, bre.12642. https://doi.org/10.1111/bre.12642

## Table of contents

# 3. Data Description

This data set includes videos depicting the surface evolution (time-lapse photographs and Particle Image Velocimetry or PIV analysis) of 38 analogue models, in five model series (A-E), simulating rift tectonics. In these experiments we examined the influence of differently oriented mantle and crustal weaknesses on rift system development during multiphase rifting (i.e. rifting involving changing divergence directions or -rates) using brittle-viscous set-ups. All experiments were performed at the Tectonic Modelling Laboratory of the University of Bern (UB).

The brittle and viscous layers, representing the upper an lower crust, were 3 cm and 1 cm thick, respectively, whereas a mantle weakness was simulated using the edge of a moving basal plate (a velocity discontinuity or VD). Crustal weaknesses were simulated using "seeds" (ridges of viscous material at the base of the brittle layers that locally weaken these brittle layers). The divergence rate for the Model A reference models was 20 mm/h so that the model duration of 2:30 h yielded a total divergence of 5 cm (so that e = 17%, given an initial model width of ca. 30 cm). Multiphase rifting model series B and C involved both a slow (10 mm/h) and fast (100 mm/h) rifting phase of 2.5 cm divergence each, for a total of 5 cm of divergence over a 2:45 h period. Multiphase rifting models series D and E had the same divergence rates (20 mm/h) as the Series A reference models, but involved both an orthogonal ($\alpha = 0^{\circ}$) and oblique rifting ($\alpha = 30^{\circ}$) phase of 2.5 cm divergence each, for a total of 5 cm of divergence over a 2:30 h period. In our models the divergence obliquity angle $\alpha$ was defined as the angle between the normal to the central model axis and the direction of divergence. The orientation and arrangements of the simulated mantle and crustal weaknesses is defined by angle $\theta$ (defined as the direction of the weakness with respect to the model axis. An overview of model parameters is provided in Table 1, and detailed descriptions of the model set-up and results, as well as the monitoring techniques can be found in Zwaan et al. (2021).

## 3.1. Monitoring of experiments

Monitoring of model evolution for all models involved time-lapse photography using a camera rig consisting of two obliquely oriented Nikon D810 (36.3 MP) cameras for stereoscopic images and a Nikon D200 camera for map view images. We applied a system with two LED lamps on both side of the model, one of which was turned on and off every 30 seconds to cast shading, accentuating structures developing at the surface of the model. Pictures were taken with every camera simultaneously over 30 second intervals, so that we obtained both a time-lapse series of fully illuminated pictures, and a time-lapse series of pictures with shading, each with 1-minute intervals. Since the Series B and C models involved changes in divergence rate, the original time-lapse intervals did not always represent the same amount of divergence. In order to standardize our model analysis, we therefore applied intervals of 5 mm of divergence (i.e. every $30^{th}$ picture for model phases involving a 10 mm/h divergence rate, every $15^{th}$ picture for models with a 20 mm/h divergence rate, and every $3^{rd}$ picture for model phases involving a 100 mm/h divergence rate.

The fully illuminated photographs with a standardized 5 mm divergence interval allowed systematic Particle Image Velocitmetry (PIV) analysis through DaVis 10.2 software from LaVision, enabling us to determine horizontal displacements and to extract incremental maximum normal strain (used as a proxy for fault activity). This PIV analysis was preferably performed on the high-resolution Nikon D810 stereoscopic photographs (after correction for their obliquity), but due to technical issues, for some models the lower resolution Nikon D200 photographs had to be used for PIV analysis (EXP856 and EXP858, the results of which were however not used in the main paper, Table 1). This difference in resolution between the Nikon D810 and D200 pictures did however not significantly affect the results of the PIV analysis as the horizontal displacements were readily recognized over a 5 mm divergence interval

We furthermore used the fully illuminated pairs of stereoscopic Nikon D810 pictures with a 5 mm divergence interval for topographic reconstructions through Agisoft Photoscan photogrammetry software. The acquired Digital Elevation Models (DEMs) were subsequently analysed in the open source QGIS software. Due to technical issues, during some model intervals or within whole models, not both of the oblique Nikon D810 pictures were available. In these cases, the Nikon D810 (or D200) map view pictures were used for topography analysis instead. Of EXP856 and EXP858, no stereoscopic pictures were available due to technical issues with the camera rig. For these experiments, the oblique pictures were made by hand at each 5 mm divergence interval using a Nikon Z6 (13.7 MP) camera instead. Overall, the slight variations in input picture quality did not significantly affect the quality of the topographic reconstructions for the purpose of this study.

*Table 1: model details*

| Model series | Model name (Zwaan et al. 2021) | Lab code | Weakness orientation | | Direction and rate of divergence | | | |
|---|---|---|---|---|---|---|---|---|
| | | | VD (angle $\theta_{VD}$) | Seeds (angle $\theta_S$) | Phase 1 (First 25 mm of divergence)* | | Phase 2 (Second 25 mm of divergence)* | |
| | | | | | Direction (angle α) | Rate (v) in mm/h | Direction (angle α) | Rate (v) in mm/h |
| **Series A*** Reference models with constant parameters | A1 | EXP828 | 0˚ | - | 0˚ | 20 | 0˚ | 20 |
| | A2 | EXP896 | 0˚ | 0˚ | 0˚ | 20 | 0˚ | 20 |
| | | *EXP895* | *0˚* | *0˚* | *0˚* | *20* | *0˚* | *20* |
| | A3 | EXP829 | 0˚ | -30˚ | 0˚ | 20 | 0˚ | 20 |
| | A4 | EXP834 | 30˚ | - | 0˚ | 20 | 0˚ | 20 |
| | A5 | EXP835 | 30˚ | 0˚ | 0˚ | 20 | 0˚ | 20 |
| | A6 | EXP838 | 30˚ | -30˚ | 0˚ | 20 | 0˚ | 20 |
| **Series B** Slow-to-fast rifting models | B1 | EXP892 | 0˚ | - | 0˚ | 10 | 0˚ | 100 |
| | B2 | EXP894 | 0˚ | 0˚ | 0˚ | 10 | 0˚ | 100 |
| | B3 | EXP849 | 0˚ | -30˚ | 0˚ | 10 | 0˚ | 100 |
| | | *EXP850* | *0˚* | *-30˚* | *0˚* | *10* | *0˚* | *100* |
| | | *EXP853* | *0˚* | *-30˚* | *0˚* | *10* | *0˚* | *100* |
| | B4 | EXP842 | 30˚ | - | 0˚ | 10 | 0˚ | 100 |
| | B5 | EXP841 | 30˚ | 0˚ | 0˚ | 10 | 0˚ | 100 |
| | B6 | EXP885 | 30˚ | -30˚ | 0˚ | 10 | 0˚ | 100 |
| | | *EXP856*** | *30˚* | *-30˚* | *0˚* | *10* | *0˚* | *100* |
| **Series C** Fast-to-slow rifting models | C1 | EXP891 | 0˚ | - | 0˚ | 100 | 0˚ | 10 |
| | C2 | EXP893 | 0˚ | 0˚ | 0˚ | 100 | 0˚ | 10 |
| | C3 | EXP851 | 0˚ | -30˚ | 0˚ | 100 | 0˚ | 10 |
| | C4 | EXP843 | 30˚ | - | 0˚ | 100 | 0˚ | 10 |
| | C5 | EXP887 | 30˚ | 0˚ | 0˚ | 100 | 0˚ | 10 |
| | | *EXP848* | *30˚* | *0˚* | *0˚* | *100* | *0˚* | *10* |
| | | *EXP888* | *30˚* | *0˚* | *0˚* | *100* | *0˚* | *10* |
| | C6 | EXP886 | 30˚ | -30˚ | 0˚ | 100 | 0˚ | 10 |
| | | *EXP884* | *30˚* | *-30˚* | *0˚* | *100* | *0˚* | *10* |
| **Series D** Orthogonal-to-oblique rifting models | D1 | EXP902 | 0˚ | - | 0˚ | 20 | 30˚ | 20 |
| | D2 | EXP904 | 0˚ | 0˚ | 0˚ | 20 | 30˚ | 20 |
| | D3 | EXP906 | 0˚ | -30˚ | 0˚ | 20 | 30˚ | 20 |
| | D4 | EXP844 | 30˚ | - | 0˚ | 20 | 30˚ | 20 |
| | | *EXP858*** | *30˚* | - | *0˚* | *20* | *30˚* | *20* |
| | D5 | EXP845 | 30˚ | 0˚ | 0˚ | 20 | 30˚ | 20 |
| | D6 | EXP889 | 30˚ | -30˚ | 0˚ | 20 | 30˚ | 20 |
| **Series E** Oblique-to-orthogonal rifting models | E1 | EXP903 | 0˚ | - | 30˚ | 20 | 0˚ | 20 |
| | E2 | EXP905 | 0˚ | 0˚ | 30˚ | 20 | 0˚ | 20 |
| | E3 | EXP907 | 0˚ | -30˚ | 30˚ | 20 | 0˚ | 20 |
| | E4 | EXP846 | 30˚ | - | 30˚ | 20 | 0˚ | 20 |
| | E5 | EXP847 | 30˚ | 0˚ | 30˚ | 20 | 0˚ | 20 |
| | E6 | EXP890 | 30˚ | -30˚ | 30˚ | 20 | 0˚ | 20 |

** Series A models were run continuously for 50 mm total divergence without change in parameters, hence in these models, phase 2 was simply a continuation of phase 1*

*** PIV analysis done on D200 (10 MP) images, and oblique pictures for photogrammetry taken by hand with a Nikon Z6 (13.7 MP) camera*

## 3.2. Data presentation

### 3.2.1. Topography evolution overviews

For each model series, we provide an overview of model topography evolution, obtained through photogrammetry analysis (Fig. 1).

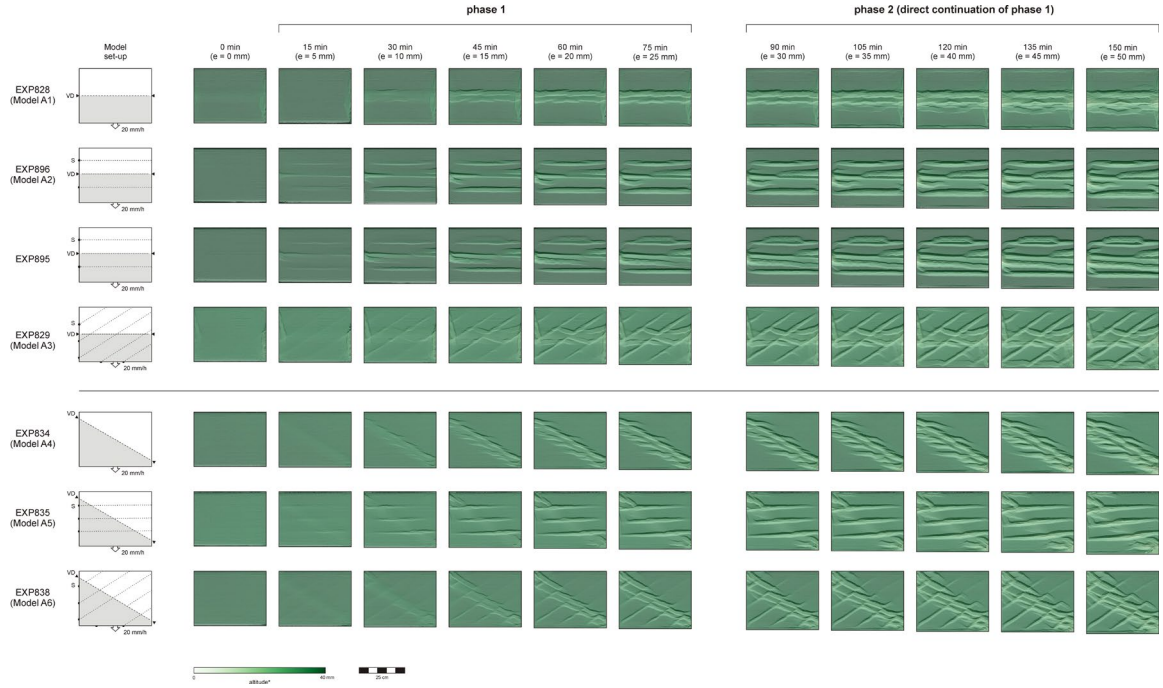


*Figure 1: Example of a topography evolution overview of the models from Series A. Each panel represents a 5 mm divergence interval.*

### 3.2.2. Topography evolution videos

Next to the topography overviews shown in section 3.2.1, we provide videos depicting the topography evolution of our models, obtained through photogrammetry analysis (Fig. 2). The frame rate is 2/s, with each frame representing a 5 mm divergence interval.

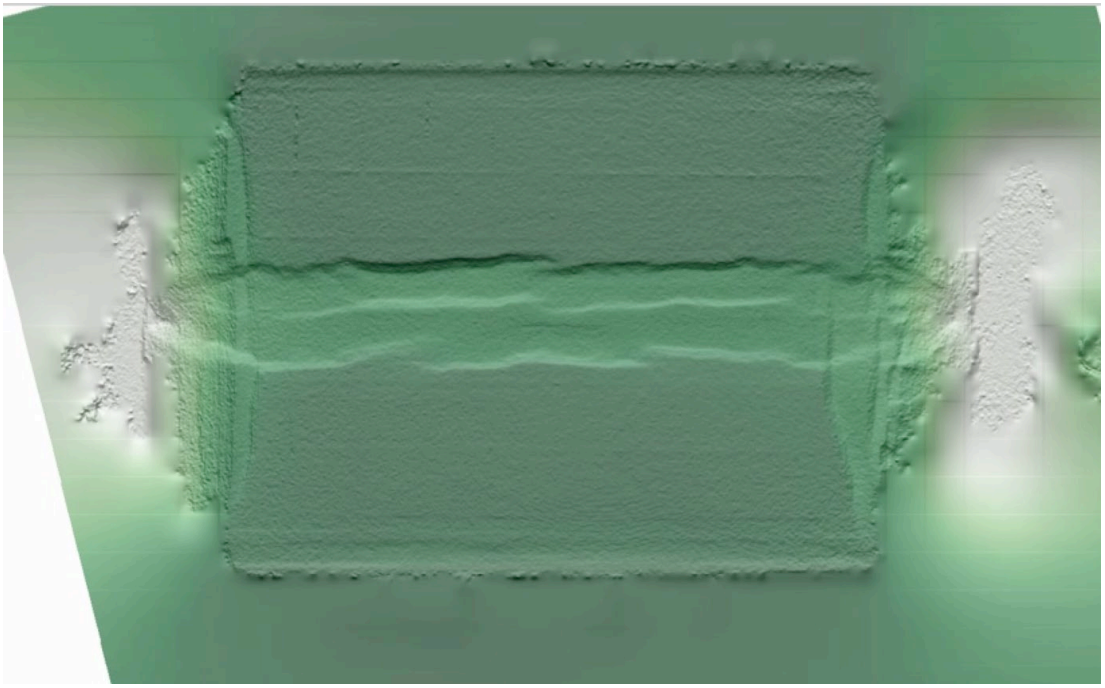

*Figure 2: Still from a video depicting the topography evolution of Model EXP828 from Series A.*

### 3.2.3. Strain evolution overviews

For each model series, we provide an overview of maximum normal strain distribution over time, obtained through PIV analysis (Fig. 3).

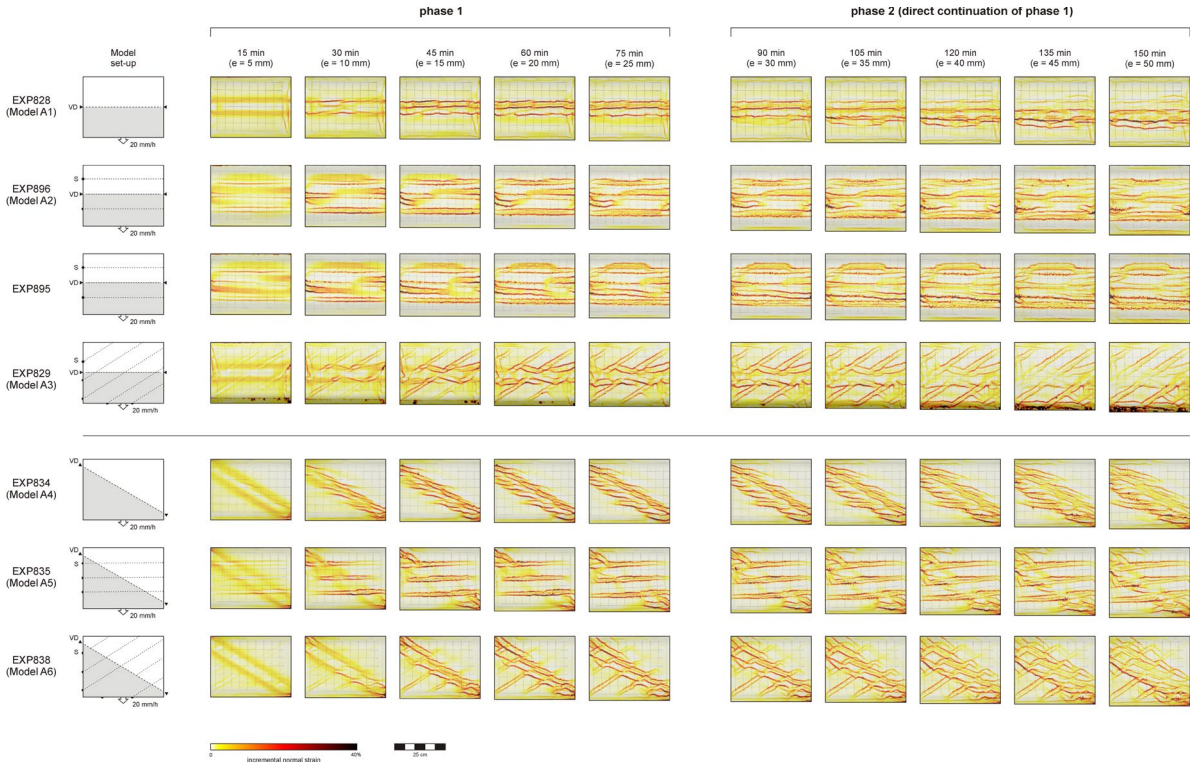


*Figure 3: Example of a maximum normal strain evolution overview of the models from Series A. Each panel represents a 5 mm divergence interval.*

### 3.2.4. Strain evolution videos

Next to the maximum normal strain overviews shown in section 3.2.3, we provide videos depicting the of maximum normal strain distribution in our models, obtained through PIV analysis (Fig. 4). The frame rate is 2/s, with each frame representing a 5 mm divergence interval.

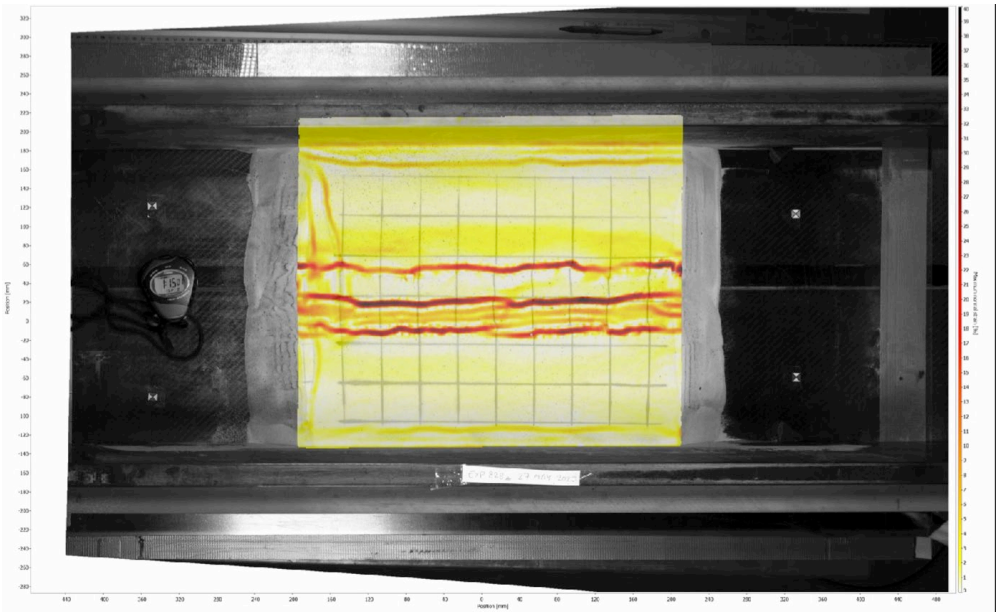

*Figure 4: Still from a video depicting the maximum normal strain evolution of Model EXP828 from Series A. Please note that the videos are rotated 180˚ with respect to the other data (i.e. in the video the upper sidewall moves instead of the lower sidewall).*

## 4. File description and visualization

For each of the five-model series the following data are provided

(i) Overview of model topography evolution (.jpeg format)

(ii) Overview of maximum normal strain evolution (.jpeg format)

For each of the 38 individual experiments the following data are provided:

(i) Topography evolution movies (.mov format)

(ii) Maximum normal strain evolution movies (.mov format)

An overview of all files of the data set is given in the **List of Files.**

## 5. Acknowledgements

We thank Timothy Schmid, Michael Rudolf, Matthias Rosenau, as well as the software engineers from LaVision (Dave Hollis, Horst Nagel, Torsten Siebert) for technical support during the PIV analysis in DaVis. We are also grateful to Kirsten Elger for her help in creating this data publication with GFZ Data Services. This research was funded by the Swiss National Science Foundation (grant 178731, http://p3.snf.ch/Project-178731).

## 6. References

Zwaan, F., Chenin, P., Erratt, D., Manatschal, G., & Schreurs, G. (2021). Competition between 3D structural inheritance and kinematics during rifting: Insights from analogue models. Basin Research, bre.12642. https://doi.org/10.1111/bre.12642